

Split superconducting and time-reversal symmetry-breaking transitions, and magnetic order in Sr_2RuO_4 under uniaxial stress

Vadim Grinenko,^{1,2,*} Shreenanda Ghosh,^{1,†} Rajib Sarkar,¹ Jean-Christophe Orain,³ Artem Nikitin,³ Matthias Elender,³ Debarchan Das,³ Zurab Guguchia,³ Felix Brückner,¹ Mark E. Barber,⁴ Joonbum Park,⁴ Naoki Kikugawa,⁵ Dmitry A. Sokolov,⁴ Jake S. Bobowski,^{6,7} Takuto Miyoshi,⁶ Yoshiteru Maeno,⁶ Andrew P. Mackenzie,^{4,8} Hubertus Luetkens,³ Clifford W. Hicks,^{4,‡} and Hans-Henning Klauss^{1,§}

¹*Institute for Solid State and Materials Physics,
Technische Universität Dresden, D-01069 Dresden, Germany*

²*IFW Dresden, Helmholtzstrasse 20, D-01069 Dresden, Germany*

³*Laboratory for Muon Spin Spectroscopy, Paul Scherrer Institute, CH-5232 Villigen PSI, Switzerland*

⁴*Max Planck Institute for Chemical Physics of Solids, D-01187 Dresden, Germany*

⁵*National Institute for Materials Science, Tsukuba 305-0003, Japan*

⁶*Department of Physics, Kyoto University, Kyoto 606-8502, Japan*

⁷*Physics, University of British Columbia, Kelowna, BC V1V 1V7, Canada*

⁸*Scottish Universities Physics Alliance (SUPA),
School of Physics and Astronomy, University of St. Andrews,
St. Andrews KY16 9SS, United Kingdom*

(Dated: February 7, 2020)

Among unconventional superconductors, Sr_2RuO_4 has become a benchmark for experimentation and theoretical analysis because its normal-state electronic structure is known with exceptional precision, and because of experimental evidence that its superconductivity has, very unusually, a spontaneous angular momentum, *i.e.* a chiral state. This hypothesis of chirality is however difficult to reconcile with recent evidence on the spin part of the order parameter. Measurements under uniaxial stress offer an ideal way to test for chirality, because under uniaxial stress the superconducting and chiral transitions are predicted to split, allowing the empirical signatures of each to be identified separately. Here, we report zero-field muon spin relaxation (ZF- μ SR) measurements on crystals placed under uniaxial stresses of up to 1.05 GPa. We report a clear stress-induced splitting between the onset tempera-

tures of superconductivity and time-reversal symmetry breaking, consistent with qualitative expectations for chiral superconductivity. We also report the appearance of unexpected bulk magnetic order under a uniaxial stress of ~ 1.0 GPa in clean Sr_2RuO_4 .

INTRODUCTION

Superconductors are classified as conventional or unconventional on the basis of whether the phase of the order parameter is isotropic in momentum space or not. Unconventional superconductivity, with sign changes in the order parameter, can have higher critical temperatures because it can be mediated by repulsive interactions that do not work in opposition to Coulomb repulsion. A very small fraction of unconventional superconductors break time reversal symmetry, in other words, have imaginary components in their order parameters. Introducing imaginary components can increase the condensation energy by filling in gap nodes, but also frustrates the pairing interaction: scattering between sections of Fermi surface where the phase of the order parameter differs by $\pi/2$ does not contribute to the condensation energy. Because superconductivity is exponentially sensitive to scattering strength, it is in general surprising when time-reversal symmetry breaking (TRSB) order parameters are favored. The origin of the superconductivity in one famous candidate for TRSB superconductivity, Sr_2RuO_4 , remains a mystery despite 25 years of intense research [1].

There is evidence that the superconductivity of Sr_2RuO_4 is chiral. A nonzero Kerr rotation is observed below the critical temperature T_c [2], and the phenomenology of junctions between Sr_2RuO_4 and conventional superconductors offers compelling evidence for domains in the superconducting state [3–5]. For most of the history of Sr_2RuO_4 evidence for chirality has been understood in terms of an odd-parity order parameter with equal spin pairing in the RuO_2 planes: $p_x \pm ip_y$ [6–9]. More recent evidence, especially a revision in NMR data, points to even-parity pairing, as in the vast majority of known superconductors [10–12]. Reconciling even parity with chirality and the tetragonal lattice symmetry of Sr_2RuO_4 compels consideration of a $d_{xz} \pm id_{yz}$ order parameter. Under conventional understanding this is an unexpected order parameter, because the line node at $k_z = 0$ appears to imply pairing of carriers *between* layers, while Sr_2RuO_4 is a layered metal with very low interlayer conductivity [6]. Indeed, the evidence on chirality is mixed. A recent junction experiment finds time-reversal invariant superconductivity [13]. Quasiparticle interference data suggest a $d_{x^2-y^2}$ gap structure [14]. Evidence for chirality has not been found in thermodynamic quantities:

as illustrated in Fig. 1, under a hypothesis of chirality T_c and T_{TRSB} , the onset temperature of time-reversal symmetry breaking, are predicted to split under uniaxial stress [15], but evidence for this splitting has not been resolved in either the stress dependence of T_c or in heat capacity data under uniaxial stress [16–18].

However there is no widely-accepted alternative hypothesis to understand the experiments that do indicate chirality. Since a confirmation of chirality may imply a new pairing mechanism it is an important point to resolve. The approach taken here is to use a non-thermodynamic probe specifically sensitive to time reversal symmetry breaking, muon spin relaxation (μSR), to test for transition splitting in samples placed under uniaxial stress. In this method, spin-polarized muons are implanted, and each muon spin then precesses in its local magnetic field. The time evolution of the polarization is determined by collecting statistics on the direction of positron emission as the muons decay. Like neutron scattering, μSR is a true bulk-sensitive probe. In contrast to neutron scattering, it offers sensitivity to spatially uncorrelated fields. The minimum detectable field is 0.01–0.1 mT, against ~ 1 mT for neutron scattering. In a small but growing number of known superconductors, muon spin polarization relaxes more quickly below T_c . This indicates onset of internal magnetic fields, and is interpreted as a signature of TRSB superconductivity. This signal is consistently seen in Sr_2RuO_4 , where the magnitude of the increase indicates a superconductivity-related internal field of ~ 0.05 mT [19–22].

Our experiment is a probe of the μSR technique as well as of Sr_2RuO_4 . The internal field is thought to arise at edges, defects, and domain walls: persistent currents are predicted to appear when spatial variation is imposed upon a TRSB order parameter [15]. This hypothesis is called into question by the fact that edge fields were not detected, to a sensitivity of $\sim 0.1 \mu\text{T}$, in scanning SQUID microscopy measurements, neither in Sr_2RuO_4 nor in another superconductor where μSR measurements indicate an internal field, $\text{PrOs}_4\text{Sb}_{12}$ [23, 24]. As μSR is the primary tool by which TRSB superconductivity has been identified in a number of other materials, clear demonstration that enhanced muon spin relaxation is not an occasional artefact of conventional superconducting transitions is vital.

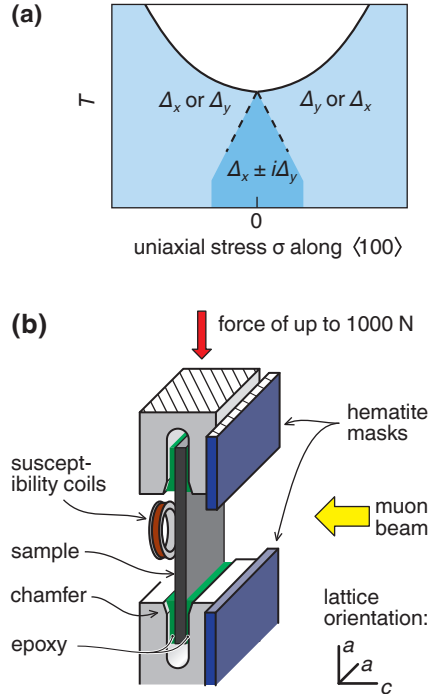


FIG. 1: **Hypothesis.** (a) Schematic uniaxial stress-temperature phase diagram for chiral superconductivity in defect-free Sr_2RuO_4 ; “ Δ_x ” stands for either p_x or d_{xz} . In the mean field approximation, T_c and T_{TRSB} for a chiral order split linearly with applied stress σ in the limit $\sigma \rightarrow 0$. We indicate a quadratic upturn in T_c at higher stresses, as seen in measurements, and do not speculate how T_{TRSB} should evolve at large $|\sigma|$. (b) Schematic of the sample setup for μSR . Hematite masks screen the portions of the holder in the beam. The chamfers are intended to smooth the stress profile and reduce shear stresses in the sample.

RESULTS ON UNSTRESSED Sr_2RuO_4

We begin by presenting the results from three samples (labelled A-C) at zero stress. Sr_2RuO_4 is grown using a floating zone technique, and growth proceeds along an in-plane lattice direction [25]. For Sample A this was approximately a $\langle 110 \rangle$ direction, and for Samples B and C a $\langle 100 \rangle$ direction. Samples A and C have critical temperatures of 1.38 and 1.35 K, respectively: close to the clean-sample limit of 1.50 K [26], while Sample B has $T_c = 1.22$ K, indicating a larger number of defects. All T_c ’s of unstressed Sr_2RuO_4 were determined by heat capacity and/or transverse-field μSR measurements, both of which are bulk-sensitive probes.

Measurements were performed with 4.2 MeV muons, which penetrate to a depth of ~ 0.1 mm, using the Dolly instrument on the $\pi\text{E}1$ beamline at the Paul Scherrer Institute. Decay positrons are counted by two detectors placed forward and backward along the incident beam direction.

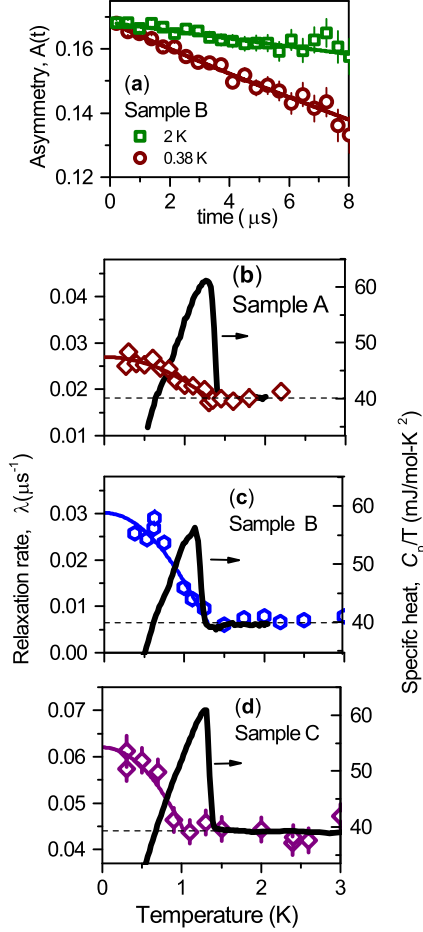


FIG. 2: **FIGURE:** (a) Example of zero-field μ SR asymmetry time spectra $A(t)$ of Sample B above and below T_{TRSB} . (b - d) Comparison of the temperature dependence of the zero field muon relaxation rate $\lambda(T)$ (left scale) and heat capacity data (right scale) for Samples A, B and C, all under zero stress. To determine T_{TRSB} , $\lambda(T)$ is fit with a quadratic form: $\lambda(T) = \lambda_0 + a[1 - (T/T_{\text{TRSB}})^2]$ for $T < T_{\text{TRSB}}$, and $\lambda(T) = \lambda_0$ for $T > T_{\text{TRSB}}$.

The asymmetry $A(t)$ in the count rate between them is proportional to the average muon spin polarization at time t . We employ a method to extract $A(t)$ from the raw count rates known as single histogram fitting (explained in the supplementary material) that reduces sensitivity to drifts in the instrumentation.

Zero-field $A(t)$ data for Sample A at two temperatures are shown in Fig. 2. Slow muon spin relaxation, due mainly to nuclear magnetic fields, is observed at the higher T , and faster relaxation at the lower T , indicating onset of an additional relaxation process. External fields are compensated to better than $1 \mu\text{T}$, so this behavior is not a consequence of appearance of vortices. The additional relaxation has an exponential form, meaning that $A(T < T_{\text{TRSB}})/A(T > T_{\text{TRSB}})$ is approximately

exponential. For a static relaxation process this quantity is a Fourier transform of the internal field distribution, and it indicates a broad field distribution characteristic of fields from dilute sources [19].

The muon spin relaxation rate λ at each temperature is obtained by fitting the following model:

$$A(T, t) = A_{\text{sam}} e^{-\lambda(T)t} + A_{\text{bkg}}.$$

A_{bkg} is a background constant to account for muons that implant into non-superconducting material such as cryostat walls, and A_{sam} is the sample signal strength. For all samples in this paper, A_{bkg} and A_{sam} are determined from transverse-field μSR measurements at a temperature well below T_c , leaving λ as the sole fitting parameter. In a field applied transverse to the muon polarization, muons in nonsuperconducting, nonmagnetic material precess in-phase, while precession in superconducting material quickly decoheres due to the field inhomogeneity introduced by the vortex lattice. These contrasting behaviours allow the two muon populations to be distinguished.

As shown in Fig. 2, a phenomenological fit to $\lambda(T)$ yields $T_{\text{TRSB}} = 1.30 \pm 0.06$ K for Sample A and 1.3 ± 0.1 K for Sample B: the same within error bars, despite Sample B's lower T_c . (All error bars in this paper are one standard deviation.) However susceptibility measurements reveal that T_c of Sample B is not homogeneous: the transition in susceptibility is broadened and 0.25 K above the transition seen in heat capacity, likely due to internal strains that locally induce higher T_c [12, 27]. For Sample C, in contrast, T_{TRSB} is 1.03 ± 0.08 K, which is below its T_c .

These measurements on unstressed Sr_2RuO_4 provide two important results. (1) The onset of enhanced muon spin relaxation is sharp; it is a transition rather than a crossover. Previously-published data sets [19–22] do not all have enough points above T_{TRSB} to resolve this. It is an important point because there is a known mechanism that can give weak exponential muon spin relaxation: fluctuations of weak ferromagnetism, as seen in YbNi_4P_2 [28] and CeFePO [29]. The distinguishing feature is that in this case the relaxation enhancement fades gradually over an order-of-magnitude increase in temperature, rather than at a transition. (2) In combination with Sample D (shown below), we observe T_{TRSB} to be within ~ 0.1 K of T_c for three samples, and to be suppressed relative to T_c for one. In combination with published results [19–22], the phenomenology appears to be that T_{TRSB} can be suppressed below T_c , but cannot exceed T_c . In attempting to resolve contradictory measurements on Sr_2RuO_4 it has been asked whether the enhanced muon spin relaxation is in fact related to the superconductivity. The combination of transition-like onset

and correlation of T_{TRSB} with T_c is strong evidence that it is.

RESULTS UNDER UNIAXIAL STRESS

Stress σ is applied along a $\langle 100 \rangle$ lattice direction, which couples strongly to the electronic structure [16]. At $\sigma = -0.7$ GPa (where $\sigma < 0$ denotes compression) there is a Fermi surface topological transition (a Lifshitz transition), at which T_c peaks at 3.5 K [12, 30]. In the limit $\sigma \rightarrow 0$ and in the mean field approximation, the ratio of the slopes $|dT_{\text{TRSB}}/d\sigma|$ and $|dT_c/d\sigma|$ is inverse to the ratios of the associated heat capacity jumps $\Delta C/T$. The experimental upper limit on the heat capacity jump at any second transition is $\sim 5\%$ of that at the superconducting transition [18], and therefore in the hypothesis figure [Fig. 1 (a)] we illustrate a steep initial $|dT_{\text{TRSB}}/d\sigma|$. The physical meaning is that under the hypothesis of chiral order, the energy difference between nonchiral and chiral superconductivity, for example p_x versus $p_x \pm ip_y$, must be small in unstressed Sr_2RuO_4 . In support of the plausibility of this circumstance, we note that weak-coupling calculations such as in Ref. [31] give nodes that have very narrow opening angles. The condensation energy gained from filling in such nodes by introducing chirality would be small.

Uniaxial stress was applied using a piezoelectric-based cell adapted to the sample size requirements for μSR , described in detail in Ref. [32]. The maximum force this cell can apply is 1000 N. The beam is ~ 1 cm in diameter, and for a decent count rate the sample area facing the beam should be at least ~ 10 mm². A schematic of a mounted sample is shown in Fig. 1(b): the sample is a plate that is thick enough both to stop the muons and to resist buckling at the highest applied stress. Hematite masks screen the portions of the sample holder exposed to the beam; the strong antiferromagnetism of hematite relaxes the polarization of muons that implant into these masks within ~ 10 ns, allowing these muons to be excluded from analysis. Being antiferromagnetic, the masks do not generate long-range stray fields. Each sample holder incorporates a force sensor based on strain gauges. Also, for most measurements a pair of concentric coils was placed behind the sample, for in situ measurement of T_c through the diamagnetic shielding of the superconducting state. Measured values of T_c were used to calibrate the force sensors following the stress dependence reported in Ref. [30]. Three samples, labelled D–F, were tested under uniaxial stress. Samples E and F were cut from Sample C.

Results are shown in Fig. 3. Sample D, with the zero-stress $T_c = 1.39$ K, was measured at 0,

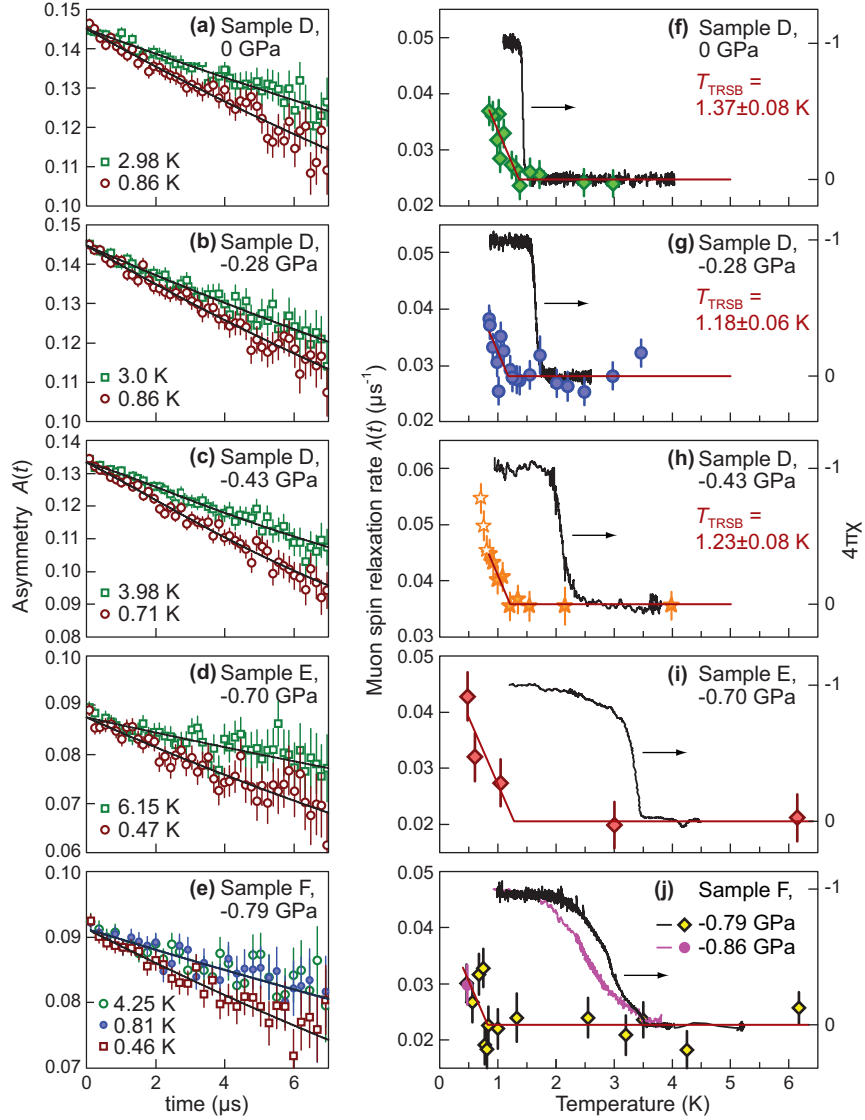


FIG. 3: Left-hand panels: Zero-field μ SR asymmetry $A(t)$ at a high temperature and at the lowest temperature reached. (a–c) Sample D at 0 GPa, -0.28 GPa and -0.43 GPa, (d) Sample E at -0.70 GPa, and (e) Sample F at -0.79 GPa plus one data point at -0.86 GPa. (Negative values denote compression.) (f–j): Temperature dependence of the muon spin relaxation rate λ , and in situ diamagnetic susceptibility data for the samples and stresses of the left-hand panels. The applied field for the susceptibility measurements was ~ 10 μ T. Heat capacity and transverse-field μ SR data show that the samples are fully superconducting, so we identify the extrema of the susceptibility signal as $4\pi\chi = 0$ and -1 . The fits to $\lambda(T)$ (red lines) are explained in the text. Note that for panels (f–h), which are all on Sample D, to avoid biasing the fit the fitting range is the same in each panel, which excludes the three open points in panel (h).

-0.28, and -0.43 GPa. A_{sam} and A_{bkg} were determined independently at each stress. The relaxation enhancement remains exponential at each stress, and it can be seen in panels (f–h) that although T_c increases under the applied stress, T_{TRSB} remains low. Because the data here do not extend to very low temperature (due to the large mass and poor thermal conductance of the pressure apparatus), a simpler, linear form is used to fit $\lambda(T)$ and extract T_{TRSB} :

$$\lambda = \begin{cases} \lambda_0 + b \times (T_{\text{TRSB}} - T), & T < T_{\text{TRSB}} \\ \lambda_0, & T > T_{\text{TRSB}} \end{cases}$$

The slope b is a common fitting parameter among all three stresses, while T_{TRSB} and λ_0 are obtained independently at each stress. This fit gives $T_{\text{TRSB}} = 1.37 \pm 0.08$ K at 0 GPa, 1.18 ± 0.06 K at -0.28 GPa, and 1.23 ± 0.08 K at -0.43 GPa. Although small, a stress dependence of T_{TRSB} is resolved: the probability that T_{TRSB} is lower at -0.28 GPa than at 0 GPa is 98%.

Samples E and F had smaller total cross-sections than Sample D, allowing higher stresses to be reached. Sample E was measured at -0.70 GPa, right at the peak in T_c , and Sample F slightly beyond, at -0.79 GPa. Adopting the same phenomenological fit as applied to Sample D, with the same slope b , T_{TRSB} of Sample F at -0.79 GPa is determined to be 0.82 ± 0.09 K. Although this is a low value, this sample was extracted from sample C, whose zero-stress T_{TRSB} was 1.03 ± 0.08 K, and we cannot firmly conclude that T_{TRSB} was suppressed by the stress. It is however clear that even when T_c is at its maximum, T_{TRSB} is low. A single data point at a yet higher stress, -0.86 GPa, indicates that the time-reversal symmetry breaking is still present.

Going further, bulk magnetic order appeared in Sample F at ~ -1.0 GPa. $A(t)$ at various temperatures is shown in Fig. 4(a): the oscillations are an unmistakable indication of long-range magnetic order. We fit the following form to $A(t)$:

$$A(t) = \alpha j_0(2\pi\gamma_\mu B_{\text{max}}t)e^{-\lambda_{\text{T}}t} + (1 - \alpha)e^{-\lambda_{\text{L}}t}.$$

Here, j_0 is a zeroth-order Bessel function, which is the Fourier transform of the Overhauser field distribution, $p(B) = 2/\pi\sqrt{B_{\text{max}}^2 - B^2}$, expected for an incommensurate spin density wave. A damped cosine form, expected for commensurate magnetic order or ferromagnetism, does not fit well. B_{max} is the magnetic hyperfine field at the peaks of the SDW, and γ_μ the muon gyromagnetic ratio. α is the oscillating signal fraction due to muons experiencing magnetic hyperfine fields transverse to the initial muon spin polarization. Since the magnetic order can also generate longitudinal field components at individual muon sites, which do not cause muon spin precession, α is a lower bound

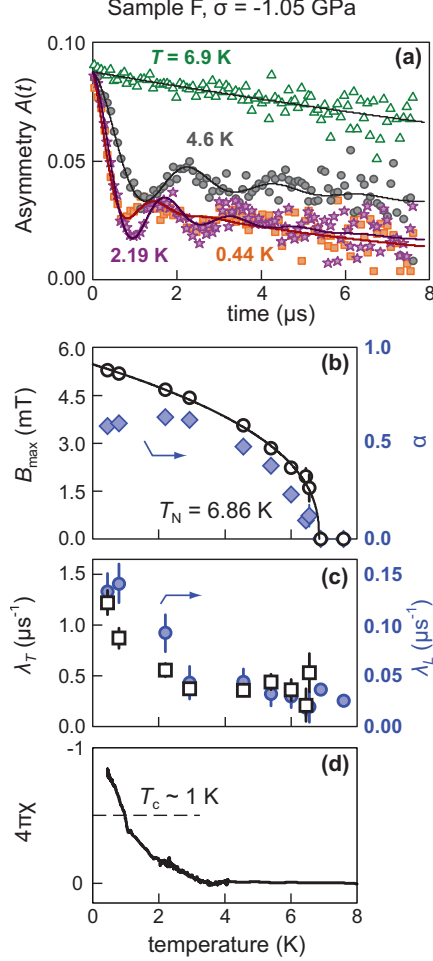


FIG. 4: **Magnetic order.** (a) Zero-field asymmetry $A(t)$ at various temperatures for Sample F at -1.05 GPa. (b) The maximum internal field B_{max} and transverse signal fraction α as a function of temperature. The fit to B_{max} gives $T_N = 6.86$ K. (c) Transverse and longitudinal relaxation rates versus temperature. Error bars, when not shown, are smaller than the symbol. (d) In situ diamagnetic susceptibility data.

for the magnetic volume fraction. λ_T and λ_L describe an additional static line broadening and a slow dynamical spin relaxation, respectively. Results of fitting are shown in Fig. 4. α saturates at $\approx 60\%$, and $B_{\text{max}}(T \rightarrow 0)$ is 5.5 ± 0.1 mT. Fitting $B_{\text{max}}(T)$ gives a Néel temperature T_N of 6.86 K. λ_T and λ_L strongly increase below ≈ 2 K. The effect can be seen directly in Fig. 4(a): more oscillations are resolvable at 2.19 than at 0.44 K. Susceptibility data [Fig. 4(d)] show that the sample is superconducting with $T_c \sim 1$ K (though with a broad transition), so we conclude that the increase in λ_T and λ_L at low temperatures is a consequence of microscopic coexistence of the superconductivity and magnetism. As further evidence that the magnetic order is a spin density wave, we note that there is no anomaly in the susceptibility data at $T \sim 7$ K that would indicate ferromagnetism.

In unstressed Sr_2RuO_4 , inelastic neutron scattering reveals strong magnetic fluctuations along columns in momentum space $q = (\pm 0.3, \pm 0.3, q_z)$, due to nesting between the α and β Fermi surfaces [33]. Substitution of a few per cent Ti on the Ru site induces static order at this \mathbf{q} , and at 9% Ti the $T \rightarrow 0$ ordered moment is $0.3 \mu_B/\text{Ru}$ [34, 35]. Although the electronic structure of Sr_2RuO_4 also introduces susceptibilities at other \mathbf{q} 's [36, 37], it is a reasonable hypothesis that the stress-induced and Ti-induced magnetic orders are related. $\text{Sr}_2\text{Ru}_{0.91}\text{Ti}_{0.09}\text{O}_4$ has been studied with muons [38]: it has $T_N \approx 20$ K, and the first minimum in $A(t)$ occurs at $\approx 0.2 \mu\text{s}$, against $\approx 1 \mu\text{s}$ for the stress-induced magnetic order here. This observation suggests an ordered moment for the stress-induced order of $\sim 0.06 \mu_B/\text{Ru}$.

In functional renormalization group calculations reported in Ref. [39], uniaxial stress was predicted to induce the formation of SDW order *before* reaching the Lifshitz transition. However, here it is clear that the magnetic order onsets beyond the Lifshitz transition: the -0.86 GPa data point of Sample F falls between the Lifshitz transition and the onset of SDW order. Our data are summarized by the phase diagram in Fig. 5.

DISCUSSION

We focus our Discussion on the observation for $|\sigma| < 1.0$ GPa of stress-induced splitting between T_c and T_{TRSB} . Splitting between T_c and T_{TRSB} has been observed previously in a few materials, but not with the clarity attained here. In UPt_3 , a splitting of ~ 0.05 K was observed [40], although enhanced muon spin relaxation was not seen at all in a later report [41]. In both $\text{Ba}_{1-x}\text{K}_x\text{Fe}_2\text{As}_2$ and $\text{Pr}_{1-x}\text{La}_x\text{Pt}_4\text{Ge}_{12}$ there is a potential splitting of a few K [42, 43], but resolution in both cases is limited by the transition widths and small scale of the increase in λ .

The splitting between T_c and T_{TRSB} rules out the possibility that enhanced muon spin relaxation is an artefact of a conventional superconducting transition. This is an especially important observation in the absence of a known microscopic mechanism that reconciles the different field scales observed in μSR and scanning SQUID magnetometry measurements. It rules out, for example, that the enhanced relaxation is a consequence of compression of flux from magnetic inclusions, present in all large Sr_2RuO_4 samples, due to Meissner screening. It rules out any mechanism based on interaction of magnetic fluctuations and conventional superconductivity.

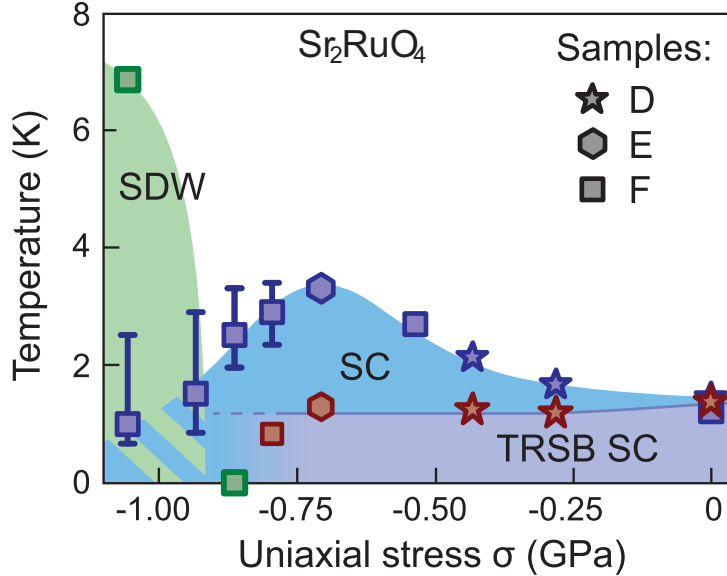


FIG. 5: Stress-temperature phase diagram of Sr_2RuO_4 based on the data presented here. For conversion to strain, the low-temperature Young’s modulus for compression along a $\langle 100 \rangle$ direction is 160 GPa [30].

There is no known magnetic mechanism that could account for the μSR data. We have noted that relaxation by weak ferromagnetic fluctuations is not consistent with the observed transition-like onset of enhanced muon spin depolarization. A glassy magnetic state could reproduce the broad distribution of fields implied by exponential relaxation, however even dilute spin glasses typically give two orders of magnitude stronger relaxation [44]. Finally, we have observed magnetic order in clean Sr_2RuO_4 at high stress, and its qualitative appearance in μSR data is completely different.

We conclude, from the correlation between T_c and T_{TRSB} in unstressed Sr_2RuO_4 and the absence of known magnetic mechanisms, that the enhanced muon spin relaxation is a property of the superconductivity. The fact that T_{TRSB} can split from T_c shows further that it is a transition of the superconducting state. This provides strong support for the hypothesis, widely accepted but not rigorously proved, that enhanced muon spin relaxation is a product of TRSB superconductivity. The observed stress-induced splitting furthermore follows qualitative expectations for chiral superconductivity in Sr_2RuO_4 . We note that recent ultrasound data [45] also indicate two-component superconductivity.

A uniaxial stress of -0.28 GPa was observed to suppress T_{TRSB} by ~ 0.2 K. Beyond this stress, T_{TRSB} appears not to evolve strongly, an observation that superficially contrasts with the prediction from Landau theory that uniaxial stress should suppress T_{TRSB} . However approaching the

Lifshitz transition is a strongly nonlinear process, and linear extrapolations based on Landau theory are unlikely to be valid at large $|\sigma|$. Stress-driven suppression of T_{TRSB} could be balanced by the overall strengthening of superconductivity. At low stresses, we note that disorder [16, 46] and fluctuations [47] are predicted to round off cusps, potentially weakening the observed stress dependence of T_{TRSB} . Under the hypothesis of chirality, we speculate further that disorder could be the mechanism that splits T_{TRSB} and T_c in some samples even at zero stress. Dislocations and inclusions are common in large samples of Sr_2RuO_4 , and the growth direction of the sample could give them a preferred orientation, lifting the tetragonal symmetry of the system.

Reconciling evidence for even-parity pairing with chirality leads to the consideration of an order parameter in the E_g representation: $d_{xz} \pm id_{yz}$. When orbital degrees of freedom are neglected it is an unexpected order parameter because the line node at $k_z = 0$ implies interlayer pairing in a metal with low k_z dispersion; its T_c is strongly suppressed in the weak-coupling calculations of Ref. [31]. To get around this difficulty, alternative TRSB order parameters without horizontal line nodes have been proposed: $d \pm is$ and $d_{x^2-y^2} \pm ig_{xy(x^2-y^2)}$. Although they depend on accidental degeneracy to obtain $T_{\text{TRSB}} \approx T_c$ on a tetragonal lattice, there is theoretical support that this may be realized in Sr_2RuO_4 [48, 49]. On the other hand, including orbital degrees of freedom allows the possibility of interorbital pairing driven by on-site Hund's rule coupling. This mechanism becomes feasible when spin-orbit and Hund's-rule couplings are non-negligible in comparison with the Fermi energy; how strong they must be is a subject of debate [50–53]. As yet, there are no widely-accepted examples of this type of superconductivity, however it allows that E_g symmetry is encoded in the local orbital degrees of freedom rather than the k dependence of the gap, such that interlayer pairing is no longer required. In Ref. [53] it is proposed that introducing momentum dependence to the spin-orbit coupling can favour interorbital E_g order in Sr_2RuO_4 .

In conclusion, the data presented here are consistent with chiral superconductivity in Sr_2RuO_4 . This is not just an unusual phase, but imposes strong qualitative constraints on models of pairing, possibly requiring a new mechanism. The superconductivity of Sr_2RuO_4 remains an important question, and we encourage further exploration.

Acknowledgement. This work has been supported financially by the Deutsche Forschungsgemeinschaft (GR 4667/1, GRK 1621, and SFB 1143 project C02) and the Max Planck Society. YM, TM, and JB acknowledge the financial support of JSPS Kakenhi (JP15H5852 and JP15K21717) and the JSPS Core-to-Core Program. NK acknowledges the financial support from JSPS Kakenhi

(No. JP18K04715) and JST-Mirai Program (No. JPMJMI18A3). AN acknowledges funding from the European Union’s Horizon 2020 research and innovation program under the Marie Skłodowska-Curie grant agreement No 701647. This work was performed partially at the Swiss Muon Source (S μ S), PSI, Villigen. We acknowledge fruitful discussions with A. Amato, E. Babaev, S. Blundell, A. Charnukha, D. Efremov, I. Eremin, C. Kallin, A. Ramires, B. Ramshaw, T. Scaffidi, C. Timm and S. Yonezawa. We also acknowledge H.-S. Xu for his contribution in the crystal growth as well as T. Shiroka and C. Wang for technical support. We thank A. Gilman, P. P. Orth, and R. M. Fernandes for results from Landau theory of a two-component order parameter.

**SUPPLEMENTARY MATERIAL: SPLIT SUPERCONDUCTING AND
TIME-REVERSAL SYMMETRY-BREAKING TRANSITIONS, AND MAGNETIC
ORDER IN Sr₂RuO₄ UNDER UNIAXIAL STRESS**

Methods

Single crystals of Sr₂RuO₄ were grown by a floating zone method [25]. With the exception of Sample C, all samples studied here were either cleaved or ground into plates, exposing the interior of the as-grown rod to the muon beam; this is technically relevant information because due to differential evaporation of Ru and Sr during the growth, the interior tends to have a higher density of inclusion phases, especially Ru, SrRuO₃, and Sr₃Ru₂O₇. Crystals grow along an in-plane direction, and to obtain samples of sufficient length for measurement under uniaxial stress we were obliged to select samples that happened to grow nearly along a $\langle 100 \rangle$ direction. Samples were mounted into holders as shown in Fig. S4 using Stycast 2850 epoxy; the epoxy layers were generally 50–100 μm thick. For Samples E and F, three additional steps were taken to improve the chances of reaching high stresses without fracturing the sample. (1) They were cut at a $\sim 10^\circ$ angle with respect to the ab plane, so that shear stresses in the sample do not align with cleave planes. (2) 10 μm -thick titanium foils were affixed to their surfaces with Stycast 1266. (3) The slots in the holder were chamfered, as shown in Fig. 1(b), to smooth the interface between the free and clamped portions of the sample.

In the μ SR system, an upstream detector triggers a timer when a muon enters the system. Muons entering the system meet one of four fates. (1) Passage through the holder without implantation. These muons are detected by a downstream veto detector, and positron counts from their decay are rejected. (2) Implantation in the hematite masks. [See Fig. 1(b).] These muons depolarize very rapidly. (3) Implantation in material other than the sample or hematite; this gives the background asymmetry A_{bkg} . (4) Implantation in the sample.

We now explain the single histogram analysis. Muon asymmetry is typically obtained through direct comparison of the count rates in two detectors. In the single-histogram analysis, data from each detector are analysed separately. This reduces sensitivity to instrumentation drifts while increasing sensitivity to background; it improves precision in determination of relative values of λ while increasing uncertainty in the absolute values.

Upon decay, emitted positrons are detected by either a forward or backward detector, and counts are binned by time after the trigger. In principle the asymmetry in the count rate, $A(t) = [N_1(t) - N_2(t)]/[N_1(t) + N_2(t)]$ where $N_i(t)$ is the number of counts in detector i at time t , is proportional to the average muon polarisation at time t . In practice, each detector has a “dark” count rate, $N_{\text{dark},i}$, that must first be subtracted from $N_i(t)$. Typically, dark rates are measured in situ, but when the relaxation is slow (as in Sr_2RuO_4) fitted relaxation rates become sensitive to errors in the dark rates. In the single histogram analysis, the $N_{\text{dark},i}$ are instead treated as fitting parameters. The counts $N_i(t)$ are fit by

$$N_i(t) = N_{0,i}[1 + A_i(t)]e^{-t/\tau_\mu} + N_{\text{dark},i},$$

where τ_μ is the muon lifetime and $N_{0,i}$ is a fitting parameter setting the overall number of synchronous (*i.e.* not dark) counts. $A_i(t)$ is a hypothesised functional form for the emission asymmetry; it has the same form for both detectors, though may have detector-dependent parameters (as indexed by the subscript i). We take $A_i(t) = A_{\text{sam},i}e^{-\lambda t} + A_{\text{bkg},i}$. λ , the relaxation rate, is determined from fits to both detector signals simultaneously, using the MUSRFIT program [54]. In this study we generally plot the combined asymmetry $A(t)$ as $A(t) \equiv \frac{1}{2}[A_1(t) - A_2(t)]$, obtaining the fitted form of $A_i(t)$ as just described and taking the experimental $A_i(t)$ as:

$$A_i(t) = \frac{N_i(t) - N_{\text{dark},i}}{N_{0,i} \exp(-t/\tau_\mu)} - 1.$$

$A_{\text{sam},i}$ and $A_{\text{bkg},i}$ need to be determined separately from transverse-field measurements, because when relaxation is slow the single histogram fits have low resolving power between these parameters

and $N_{\text{dark},i}$.

For simplicity, a non-relaxing background A_{bkg} was assumed for all samples. This is not strictly correct. For example, between -0.28 and -0.43 GPa a chip broke from Sample D, exposing some brass material of the ac susceptibility coil holder, which is relaxing due to the nuclear magnetic moments of Cu. If instead A_{bkg} is taken to relax following an assumed functional form, the single histogram analysis gives different absolute values for λ . This is the reason why the fit procedure introduces an uncertainty on the absolute value of λ . We show below that assuming different backgrounds has no substantial effect on temperature-dependent changes in λ .

Although here we fit zero-field μSR time spectra to simple exponential decays, it is also common to analyse zero-field time spectra by $A(t) = A_{\text{bkg}} + A_{\text{sample}} \times f_{\text{GKT}}(t) \times e^{-\lambda t}$, where f_{GKT} is the Gauss-Kubo-Toyabe function, $\text{GKT} = \frac{1}{3} + \frac{2}{3}(1 - \sigma^2 t^2) \exp(-\frac{1}{2}\sigma^2 t^2)$. In principle, f_{GKT} is the contribution from dense sources such as nuclear dipoles, and $e^{-\lambda t}$ the contribution from dilute sources. We tested a simpler phenomenological form on Sample D, $A(t) = A_{\text{bkg}} + A_{\text{sam}} \exp(-\lambda t) \exp(-\frac{1}{2}\sigma^2 t^2)$, but found that the fit quality was not improved by the added parameter.

Effect of the background in the single histogram analysis

Before each zero field measurements the ratio $A_{\text{bkg}}/A_{\text{sam}}$ was determined using transverse field μSR . In Fig. S1 transverse-field data from Sample D at 0 and -0.43 GPa are shown. Above T_c the muons precess without relaxation in the applied 14.5 mT field. The field was applied along the c axis, where $H_{c2}(T \rightarrow 0) \approx 70$ mT, and below T_c the field within the sample becomes highly inhomogeneous due to the vortex lattice. Correspondingly, the polarization of muons implanted in the sample relaxes rapidly. At -0.43 GPa, it can be seen however that there is residual oscillation that appears not to relax. This is due to the background muons; as noted above, a chip broke from the sample between -0.28 and -0.43 GPa, exposing some of the susceptibility coil holder (which was made of brass). To fit $A(t)$, we assume a field distribution that is a sum of a few Gaussians, with one describing the background and the rest the vortex lattice [55]. $A(t)$ is fitted in the time domain to a Fourier transform of this assumed field distribution. Results are shown in panels (c) and (d). By comparing the fitted amplitudes of the background and vortex contributions, we obtain $A_{\text{bkg}}/A_{\text{sam}} \approx 0.12$ at -0.43 GPa, and 0.05 at 0 and -0.28 GPa. For the remaining samples,

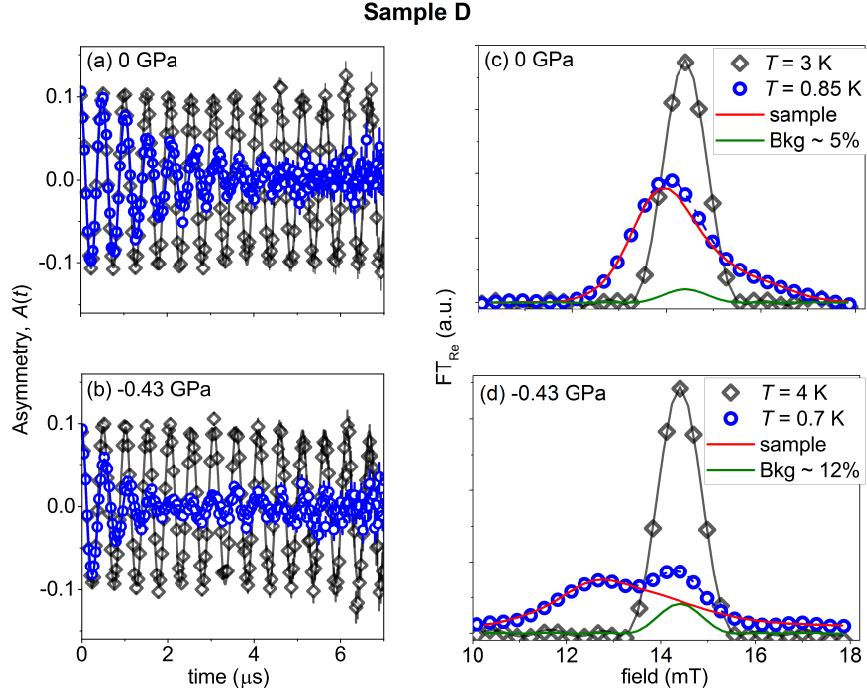


FIG. S1: **(a-b)** Transverse-field μ SR time spectra above and below T_c , with a muon spin polarization 45° with respect to the sample c axis \hat{c} and $\mathbf{B} \parallel \hat{c}$. **(c-d)** Fourier transforms of the time spectra shown in panels (a) and (b). The fit to determine the sample contribution is done in the time domain.

$A_{\text{bkg}}/A_{\text{sam}}$ came to ≈ 0 for Samples A, B, and F; ≈ 0.12 for Sample C; and ≈ 0.15 for Sample E.

It was noted above that the single histogram analysis introduces uncertainty into absolute values of λ , but not into temperature-dependent changes. We provide further details here. We show that taking a relaxing background, due to possible magnetism in the background material, shifts the absolute values of λ obtained from the single histogram analysis, but does not substantially affect relative values.

The effect will have been particularly notable for Sample D at -0.43 GPa: the exposed brass is relaxing due to Cu nuclear magnetic moments. The relaxation from copper can be accurately fit by the Gauss-Kubo-Toyabe form with $\sigma = 0.39 \mu\text{s}^{-1}$ [56]. In Fig. S2(a) we show results for $A(t)$ taking 20% of the background to relax the muon spins as copper does, and the remaining 80% to be non-relaxing. This alters the fitted values of $N_{\text{dark},i}$, and so also the resulting $A(t)$. Panel (b) shows λ extracted from the single histogram analysis with a non-relaxing background, this 20% background, and also a 55% background. The 20% copper case is seen to reduce λ for $T > T_{\text{TRSB}}$ to a similar value as obtained for 0 and -0.28 GPa; because the background was

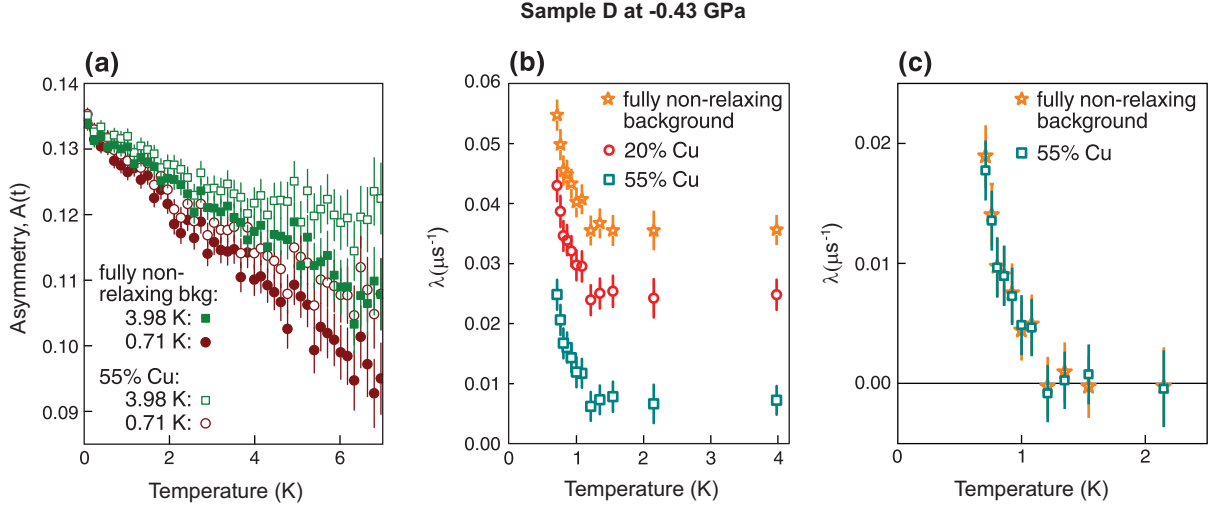


FIG. S2: **Testing different backgrounds.** (a) $A(t)$ resulting from the single histogram analysis of Sample D when a non-relaxing background term is assumed, and when a 55% of the background is assumed to relax muon polarization following, as expected for copper, the Kubo-Toyabe formula with $\sigma = 0.39 \mu\text{s}^{-1}$. (b) Results for the relaxation rate λ taking different portions of copper in the background. The dominant effect of adding a relaxing element to the background is a uniform shift downward. (c) There is essentially no effect on temperature-dependent relative changes in λ extracted from the analysis.

smaller for 0 and -0.28 GPa, these two measurements are more likely to yield correct absolute values. The important point is revealed in panel (c): for all of these assumed backgrounds, the effect on temperature-dependent relative values of λ extracted from the single histogram analysis is negligible.

Analysis of the ZF μSR data in the magnetic state

To describe the internal field distribution in the magnetic state we used the Bessel function as discussed in the main text. This field distribution is consistent with an incommensurate magnetic structure indicating a SDW state. It would also be a reasonable hypothesis that tuning Sr_2RuO_4 to peaks in the density of states induces ferromagnetism. Therefore, we show here that ferromagnetism does not give a good match to the data. The expected functional form for $A(t)$ for ferromagnetism is a cosine:

$$A(t) = \alpha \cos(2\pi\gamma_\mu Bt) e^{-\lambda_T t} + (1 - \alpha) e^{-\lambda_L t},$$

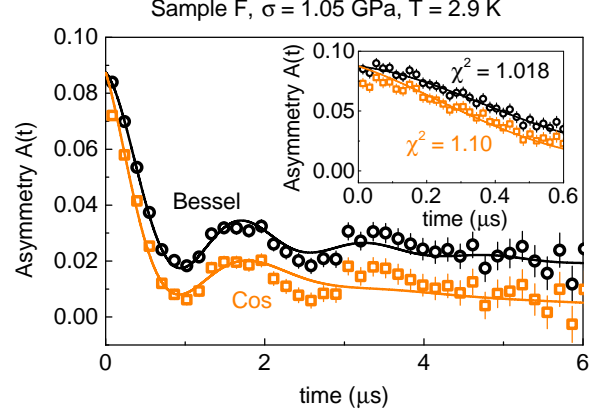


FIG. S3: **Testing different models to describe magnetic order.** Zero-field asymmetry $A(t)$ in the magnetic state for Sample F at -1.05 GPa, fitted with a Bessel function describing incommensurate spin density wave order, and a damped cosine describing ferromagnetism or commensurate magnetic order. The Bessel function is seen to give a better fit; the cosine fit does not capture oscillations after $\sim 2 \mu\text{s}$. Note that in the single histogram analysis a functional form for $A(t)$ must be assumed to fit the dark count rate, which results in separate data values for the two forms. Both are derived from a single data set.

where B is now the average local magnetic field at the muon site induced by the magnetism, and other quantities are as in the main text. This form also applies to commensurate magnetic order: reversing the field direction on every other site would not alter $A(t)$. Results are shown in Fig. S3. It is seen that the cosine fit does not work as well: it does not reproduce the data at early time ($t \lesssim 0.1 \mu\text{s}$) or at $t > 2 \mu\text{s}$. In particular, it does not capture the third peak in $A(t)$, at $t \approx 3.2 \mu\text{s}$, which is clearly present not only here (at $T = 2.9 \text{ K}$), but also in the 2.19 and 4.4 K data in Fig. 4(a).

Analysis of heat capacity jumps

The hypothesized phase diagram, Fig. 1(a), indicates a slope $|dT_{\text{TRSB}}/d\sigma|$, where σ is stress applied along a $\langle 100 \rangle$ lattice direction, that, for consistency with heat capacity data under uniaxial stress [18], far exceeds $|dT_c/d\sigma|$. Here, we explain further.

We take a general free energy

$$F_0 = \frac{a}{2} (\Delta_x^2 + \Delta_y^2) + \frac{u}{4} (\Delta_x^4 + \Delta_y^4) + \frac{\beta}{2} \Delta_x^2 \Delta_y^2 + \frac{\alpha}{2} \Delta_x^2 \Delta_y^2 \cos(2\theta) + \frac{g\sigma}{2} (\Delta_x^2 - \Delta_y^2).$$

Δ_x and Δ_y are respectively the amplitudes of the x and y components of the gap function, and θ

is the phase difference between them. σ is the applied uniaxial stress, and g a coupling constant. $a = a_0(T - T_{c,0})$.

For a chiral state to occur, we require $\alpha > 0$ to ensure that the energy is minimized for $\theta = \pm\pi/2$, and $|\beta - \alpha| < u$ to ensure that both Δ_x and Δ_y become nonzero below $T_{c,0}$ in the unstrained sample. To obtain the mean-field phase diagram, this free energy is minimized with respect to Δ_x , Δ_y , and θ ; the minimization with respect to θ gives $\theta = \pm\pi/2$. This minimization gives a heat capacity jump at $T_{c,0}$ of

$$\frac{\Delta C_0}{T_{c,0}} = \frac{a_0^2}{u + \beta - \alpha}.$$

When $\sigma \neq 0$, the transition splits into two transitions,

$$\begin{aligned} T_c &= T_{c,0} + \frac{g|\sigma|}{a_0}, \\ T_{\text{TRSB}} &= T_{c,0} - \frac{g|\sigma|}{a_0} \frac{u + \beta - \alpha}{u - \beta + \alpha}. \end{aligned}$$

The heat capacity jumps at these two transitions are

$$\begin{aligned} \frac{\Delta C_1}{T_c} &= \frac{a_0^2}{2u}, \\ \frac{\Delta C_2}{T_{\text{TRSB}}} &= \frac{a_0^2}{2u} \frac{u - \beta + \alpha}{u + \beta - \alpha}, \end{aligned}$$

where ΔC_1 is the heat capacity jump at T_c , and ΔC_2 that at T_{TRSB} . These expressions give:

$$\frac{\Delta C_1}{T_c} \frac{dT_c}{d|\sigma|} = - \frac{\Delta C_2}{T_{\text{TRSB}}} \frac{dT_{\text{TRSB}}}{d|\sigma|} = \frac{a_0 g}{2u}.$$

In other words, in the mean field approximation the ratio of the slopes $dT_c/d|\sigma|$ and $dT_{\text{TRSB}}/d|\sigma|$ is inverse to the heat capacity jumps $\Delta C/T$ at the transitions.

More information on the sample and cell configuration

We provide here a brief description of the apparatus, and more information on the sample configuration. The uniaxial stress apparatus is explained fully in Ref. [32]. To facilitate sample exchange, samples are mounted in detachable holders that slot into a piezoelectric-driven device that we term the generator. The generator contains a compression spring that generates a preload force of ~ 1000 N. This preload is applied to two sets of piezoelectric actuators. One set is anchored to the cell frame and the other to the sample. By adjusting the relative lengths of the actuators

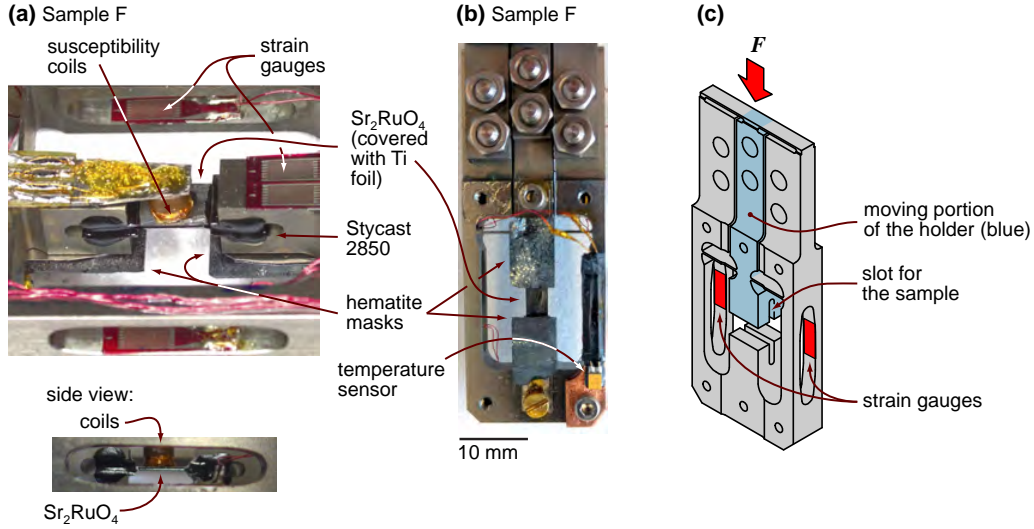


FIG. S4: (a) Photographs of sample F, showing the location of the ac susceptibility coil, the hematite masks, and the force-sensing strain gauges. (b) A view from the muon direction for the same sample. The beam diameter is ~ 1 cm. (c) Schematic of the sample holder showing the moving portion of the holder (blue color), slots for the sample and the strain gauges to measure the applied force. The other strain gauges visible in panel (a) are used to complete the Wheatstone bridge.

through the applied voltages, the fraction of the preload that is applied to the sample is varied. The cell is designed such that it can only apply compressive forces; it incorporates a mechanical interface that opens when the applied displacement becomes tensile. The generator incorporates a strain gauge bridge that is configured to measure the displacement applied to the sample holder. This sensor serves as a complement to the strain gauge-based force sensor incorporated into the holder. (The strain gauges were supplied by Tokyo Sokki, part number CFLA-3-350-11.) force-displacement relation is linear then the deformation of the sample, and epoxy anchoring the sample, is elastic. On the other hand a sharp increase in displacement accompanied by a decrease in force indicates that a fracture or slip occurred somewhere.

Fig. S4 shows a closer view of sample F, as mounted for measurement. As has been described in the main text and above, there is a pair of coils for in situ measurement of T_c through magnetic susceptibility. The two coils each have ≈ 100 turns, and are wound directly on top of each other onto the same form. Together, they had an inner diameter of ≈ 1.8 mm and an outer diameter of ≈ 2.8 mm, and extended from ≈ 0.4 to 1.0 mm above the sample. The measurement is of the mutual inductance of the two coils using a lock-in amplifier, and the excitation field applied at the sample surface was typically $\sim 10 \mu\text{T}$.

The loading curves, meaning the readings from the force and displacement sensors, for samples D–F are shown in Fig. S5. All samples were cooled with the piezoelectric actuators grounded. The readings of the sensors with no force on the sample could be straightforwardly determined by shifting the actuators towards tensile force: when the force reaches zero and the mechanical interface opens, the sensor readings plateau (0 GPa label in Fig. S5). All samples were under modest compression after initial cool-down; we speculate that this is due to differential thermal contraction between loaded and unloaded piezoelectric actuators. For sample D, there is a prominent anomaly in the loading curve between -0.28 and -0.43 GPa, which is where a chip broke from the sample (see inset of Fig. S5). The chip will have reduced the homogeneity of the applied stress, however the susceptibility data in Fig. 3(h) show that in spite of it the superconducting transition at -0.43 GPa was not excessively broad. The loading curves for samples E and F, in contrast, show no such anomalies. The loading data for Sample F fall on two distinct lines. We speculate that this was caused by a slip at the holder-generator interface, or elsewhere in the generator, that shifted the calibration of the displacement sensor. After pulling the sample out of the system no visible signs of damage to the sample were found.

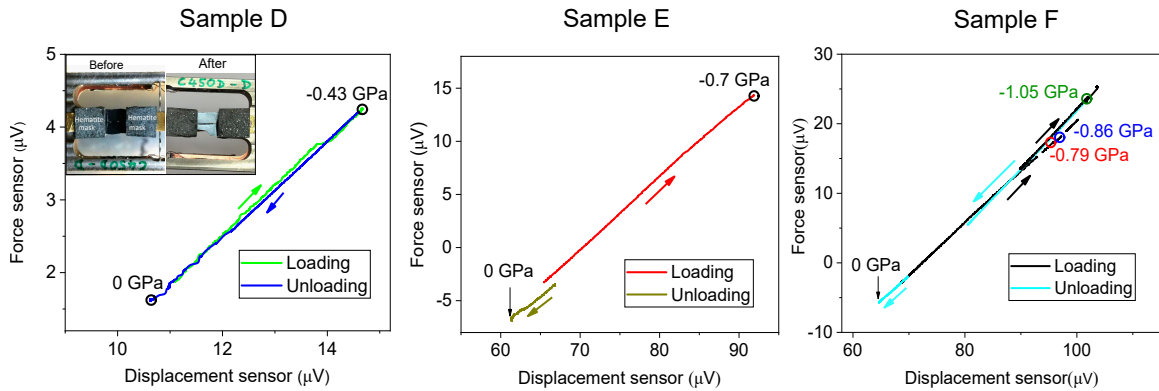


FIG. S5: **Loading curves:** In situ force and displacement sensor readings. A linear dependence indicates elastic sample deformation. An anomaly in the loading curve for Sample D is where a chip broke from the sample. Circles indicate the positions of μ SR measurements; stress values were obtained from the known stress dependence of T_c , and negative values indicate compression.

The force sensor was calibrated for each sample using the known stress dependence of T_c [30]. For Samples D and F, T_c was identified as the midpoint of the transition in susceptibility; due to the width of the superconducting transition near the Lifshitz transition, only data with $|\sigma| < 0.53$ GPa were used. Sample E was tuned to the maximum T_c , reported in Ref. [30] to occur at -0.70 GPa.

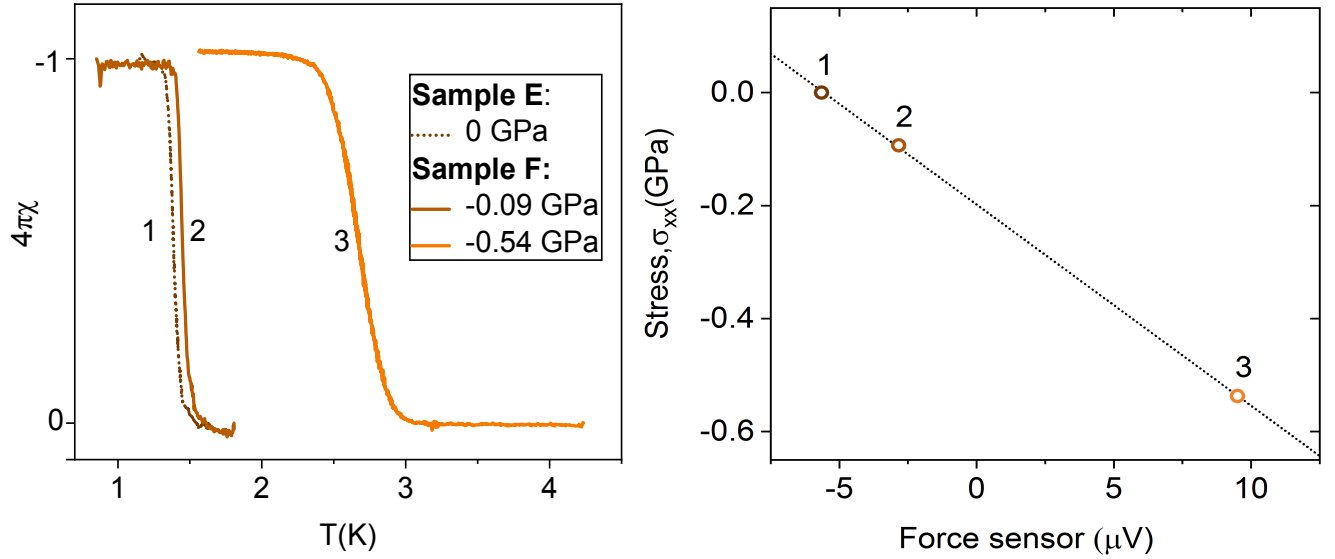


FIG. S6: **Calculating the stress:** (Left panel) ACS curves measured in-situ at different stress values below the peak in T_c for Sample E and F. (Right panel) Force sensor calibration for sample F. The 0 GPa value is taken from T_c of Sample E, which was immediately adjacent to Sample F in the original rod.

Sample characterization

Additional characterization data of the samples are shown in Fig. S7. Heat capacity data are shown for all samples except Sample F; Samples E and F were both drawn from Sample C, and so are expected to have very similar properties. The samples have sharp transitions with T_c near the clean-sample limit of 1.50 K in all samples except Sample B. For Samples D and E, T_c and the transition widths obtained from heat capacity and susceptibility data match closely, indicating high sample homogeneity, while for Sample B the transition in susceptibility is broad and at a higher temperature than the heat capacity transition, most likely due to internal defects such as Ru inclusions, which locally increase T_c through strain effects.

To obtain a superconducting penetration depth we performed transverse field measurements at different temperatures similar to shown in Fig. S1. In the superconducting state the data were analyzed by a multi-Gaussian fit to obtain the second moment of the internal field distribution in the vortex state as described in Ref. [55]. The penetration depth λ was calculated using Brandt relation between the magnetic penetration depth and the second moment $\langle \Delta B^2 \rangle = 0.00371 \Phi_0^2 / \lambda^4$, where Φ_0 is the magnetic flux quantum, valid for the case when the applied field $B \ll B_{c2}$ [57]. The

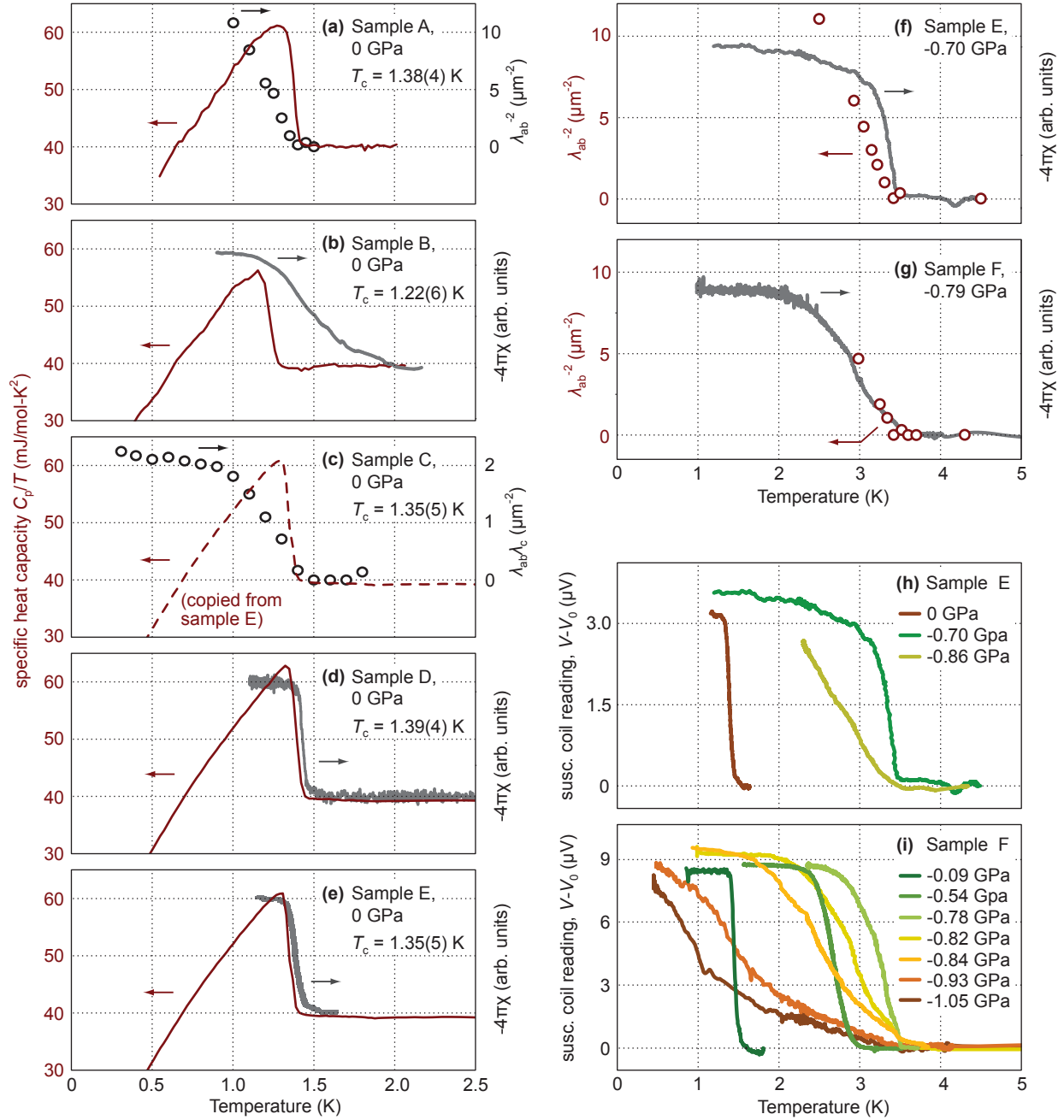


FIG. S7: **Further characterization of the samples:** All susceptibility data were recorded in-situ. Penetration depths were determined through transverse-field μ SR. Heat capacity data for Samples C, D, and E were recorded from portions of the samples that were removed from the holder after the μ SR measurement, for Sample A the measurement was performed on a portion of the sample before the μ SR measurement. Note that for Sample C, we show heat capacity data from Sample E, which was extracted from Sample C. Panels (h) and (i) show ac susceptibility raw voltage data at different uniaxial stresses without normalization.

latter holds for the data presented in Fig.S7, where the inverse squared penetration depth λ^{-2} is plotted. The measurements shown in panel (a), (f), and (g) were performed in $B \parallel c = 2$ mT and in panel (c) in $B \parallel ab = 14.5$ mT. Like the heat capacity data of Ref. [18], these measurements show definitively that the strain-induced increase in T_c is a bulk effect.

Finally, we summarize all measured in-situ susceptibility data for samples E and F in Fig. S7 **(h)** and **(i)** . Note that in these panels the raw Lock-In-amplifier voltage data are shown without normalization, the offset voltage V_0 above T_c being subtracted from each curve. These data demonstrate that at all measured uniaxial stress values the superconducting volume fraction at lowest temperatures is ≈ 1 .

* Electronic address: v.grinenko@ifw-dresden.de; These authors contributed equally.

† These authors contributed equally.

‡ Electronic address: hicks@cpfs.mpg.de

§ Electronic address: henning.klauss@tu-dresden.de

- [1] Y. Maeno, H. Hashimoto, K. Yoshida, S. Nishizaki, T. Fujita, J. Bednorz, and F. Lichtenberg, *Nature* **372**, 532 (1994).
- [2] J. Xia, Y. Maeno, P. T. Beyersdorf, M. M. Fejer, and A. Kapitulnik, *Physical Review Letters* **97**, 167002 (2006).
- [3] F. Kidwingira, J. D. Strand, D. J. Van Harlingen, and Y. Maeno, *Science* **314**, 1267 (2006).
- [4] T. Nakamura, T. Sumi, S. Yonezawa, T. Terashima, M. Sigrist, H. Kaneyasu, and Y. Maeno, *Journal of the Physical Society of Japan* **81**, 064708 (2012).
- [5] M. A. Anwar, T. Nakamura, S. Yonezawa, M. Yakabe, R. Ishiguro, H. Takayanagi, and Y. Maeno, *Scientific Reports* **3**, 2480 (2013).
- [6] A. P. Mackenzie and Y. Maeno, *Reviews of Modern Physics* **75**, 657 (2003).
- [7] Y. Maeno, S. Kittaka, T. Nomura, S. Yonezawa, and K. Ishida, *Journal of the Physical Society of Japan* **81**, 011009 (2012).
- [8] C. Kallin, *Reports on Progress in Physics* **75**, 042501 (2012).
- [9] A. P. Mackenzie, T. Scaffidi, C. W. Hicks, and Y. Maeno, *npj Quantum Materials* **2**, 40 (2017).
- [10] A. Pustogow, Y. Luo, A. Chronister, S. Y.-S., D. A. Sokolov, F. Jerzembeck, A. P. Mackenzie, C. W. Hicks, N. Kikugawa, S. Raghu, et al., *Nature* **574**, 72 (2019).
- [11] K. Ishida, M. Manago, and Y. Maeno, arXiv.1907.12236 (2019).
- [12] A. Steppke, L. Zhao, M. E. Barber, T. Scaffidi, F. Jerzembeck, H. Rosner, A. S. Gibbs, Y. Maeno, S. H. Simon, A. P. Mackenzie, et al., *Science* **355**, eaaf9398 (2017).
- [13] S. Kashiwaya, K. Saitoh, H. Kashiwaya, M. Koyanagi, M. Sato, K. Yada, Y. Tanaka, and Y. Maeno,

- Physical Review B **100**, 094530 (2019).
- [14] R. Sharma, S. D. Edkins, W. Z., A. Kostin, C. Saw, Y. Maeno, A. P. Mackenzie, J. C. Davis, and M. V., Arxiv: 1912.02798 (2019).
- [15] M. Sigrist and K. Ueda, Reviews of Modern Physics **63**, 239 (1991).
- [16] C. W. Hicks, D. O. Brodsky, E. A. Yelland, A. S. Gibbs, J. A. N. Bruin, M. E. Barber, S. D. Edkins, K. Nishimura, S. Yonezawa, Y. Maeno, et al., Science **344**, 283 (2014).
- [17] C. A. Watson, A. S. Gibbs, A. P. Mackenzie, C. W. Hicks, and K. A. Moler, Physical Review B **98**, 094521 (2018).
- [18] Y.-S. Li, N. Kikugawa, D. A. Sokolov, F. Jerzembeck, A. S. Gibbs, Y. Maeno, C. W. Hicks, M. Nicklas, and A. P. Mackenzie, arXiv (2019).
- [19] G. M. Luke, Y. Fudamoto, K. M. Kojima, M. I. Larkin, J. Merrin, B. Nachumi, Y. J. Uemura, Y. Maeno, Z. Q. Mao, Y. Mori, et al., Nature **394**, 558 (1998).
- [20] G. M. Luke, Y. Fudamoto, K. M. Kojima, M. I. Larkin, B. Nachumi, Y. J. Uemura, J. E. Sonier, Y. Maeno, Z. Q. Mao, Y. Mori, et al., Physica B **289-290**, 373 (2000).
- [21] T. Shiroka, R. Fittipaldi, M. Cuocco, R. De Renzi, Y. Maeno, R. J. Lycett, S. Ramos, E. M. Forgan, C. Baines, A. Rost, et al., Physical Review B **85**, 134527 (2012).
- [22] W. Higemoto, A. Koda, R. Kadono, Y. Yoshida, and Y. Onuki, JPS Conference Proceedings **2**, 010202 (2014).
- [23] J. R. Kirtley, C. Kallin, C. W. Hicks, E.-A. Kim, Y. Liu, K. A. Moler, Y. Maeno, and K. D. Nelson, Physical Review B **76**, 014526 (2007).
- [24] C. W. Hicks, J. R. Kirtley, T. M. Lippman, N. C. Koshnick, M. E. Huber, Y. Maeno, W. M. Yuhasz, M. B. Maple, and K. A. Moler, Physical Review B **81**, 214501 (2010).
- [25] J. S. Bobowski, N. Kikugawa, T. Miyoshi, H. Suwa, H.-S. Xu, S. Yonezawa, D. A. Sokolov, A. P. Mackenzie, and Y. Maeno, Condensed Matter **4**, 6 (2019).
- [26] A. P. Mackenzie, R. K. W. Haselwimmer, A. W. Tyler, G. G. Lonzarich, Y. Mory, S. Nishizaki, and Y. Maeno, Physical Review Letters **80**, 161 (1998).
- [27] Y. Maeno, T. Ando, Y. Mori, E. Ohmichi, S. Ikeda, S. Nishizaki, and S. Nakatsuji, Physical Review Letters **81**, 3765 (1998).
- [28] J. Spehling, M. Günther, C. Krellner, N. Yèche, H. Luetkens, C. Baines, C. Geibel, and H.-H. Klauss, Physical Review B **85**, 140406(R) (2012).
- [29] S. Lausberg, J. Spehling, A. Steppke, A. Jesche, H. Luetkens, A. Amato, C. Baines, C. Krellner, M. Brando, C. Geibel, et al., Physical Review Letters **109**, 216402 (2012).
- [30] M. E. Barber, F. Lechermann, S. V. Streltsov, S. L. Skornyakov, S. Ghosh, B. J. Ramshaw, N. Kikugawa, D. A. Sokolov, A. P. Mackenzie, C. W. Hicks, et al., Physical Review B **100**, 245139 (2019).
- [31] H. S. Røising, T. Scaffidi, F. Flicker, G. F. Lange, and S. H. Simon, Physical Review Research **1**, 033108 (2019).
- [32] C. W. Hicks, S. Ghosh, M. E. Barber, and H.-H. Klauss, JPS Conf. Proc. **21**, 011040 (2018).

- [33] Y. Sidis, M. Braden, P. Bourges, B. Hennion, S. Nishizaki, Y. Maeno, and Y. Mori, *Physical Review Letters* **83**, 3320 (1999).
- [34] M. Minakata and Y. Maeno, *Physical Review B* **63**, 180504 (2001).
- [35] M. Braden, O. Friedt, Y. Sidis, P. Bourges, M. Minakata, and Y. Maeno, *Physical Review Letters* **88**, 197002 (2002).
- [36] P. Steffens, Y. Sidis, J. Kulda, Z. Q. Mao, Y. Maeno, I. I. Mazin, and M. Braden, *Physical Review Letters* **122**, 047004 (2019).
- [37] S. Cobo, F. Ahn, I. Eremin, and A. Akbari, *Physical Review B* **94**, 224507 (2016).
- [38] J. P. Carlo, T. Goko, I. M. Gat-Malureanu, P. L. Russo, A. T. Savici, A. A. Aczel, G. J. MacDougall, J. A. Rodriguez, T. J. Williams, G. M. Luke, et al., *Nature Materials* **11**, 323 (2012).
- [39] Y.-C. Liu, F.-C. Zhang, T. M. Rice, and Q.-H. Wang, *npj Quantum Materials* **2**, 12 (2017).
- [40] G. M. Luke, A. Keren, L. P. Le, W. D. Wu, Y. J. Uemura, D. A. Bonn, L. Taillefer, and J. D. Garrett, *Physical Review Letters* **71**, 1466 (1993).
- [41] P. Dalmas de Réotier, A. Huxley, A. Yaouanc, J. Flouquet, P. Bonville, P. Imbert, P. Pari, P. C. M. Gubbens, and A. M. Mulders, *Physics Letters A* **205**, 239 (1995).
- [42] V. Grinenko, P. Materne, R. Sarkar, H. Luetkens, K. Kihou, C. H. Lee, S. Akhmadaliev, D. V. Efremov, S.-L. Drechsler, and H.-H. Klauss, *Physical Review B* **95**, 214511 (2017).
- [43] J. Zhang, Z. F. Ding, K. Huang, C. Tan, A. D. Hillier, P. K. Biswas, D. E. MacLaughlin, and L. Shu, *Physical Review B* **100**, 024508 (2019).
- [44] W. D. Wu, A. Keren, L. P. Le, G. M. Luke, B. J. Sternlieb, Y. J. Uemura, C. L. Seaman, Y. Dalichaouch, and M. B. Maple, *Physical Review Letters* **72**, 3722 (1994).
- [45] S. Ghosh, A. Shekhter, F. Jerzembeck, N. Kikugawa, D. A. Sokolov, A. P. Mackenzie, C. W. Hicks, and B. J. Ramshaw, In preparation (2020).
- [46] Y. Yu and S. Raghu, *Physical Review B* **100**, 094517 (2019).
- [47] M. H. Fischer and E. Berg, *Physical Review B* **93**, 054501 (2016).
- [48] A. T. Rømer, D. D. Scherer, I. M. Eremin, P. J. Hirschfeld, and B. M. Andersen, *Physical Review Letters* **123**, 247001 (2019).
- [49] S. A. Kivelson, A. C. Yuan, B. J. Ramshaw, and R. Thomale, In preparation (2020).
- [50] C. M. Puetter and H.-Y. Kee, *Europhysics Letters* **98** (2012).
- [51] S. Hoshino and P. Werner, *Physical Review Letters* **115**, 247001 (2015).
- [52] A. Ramires and M. Sigrist, *Physical Review B* **100**, 104501 (2019).
- [53] H. G. Suh, H. Menke, P. M. R. Brydon, C. Timm, A. Ramires, and D. F. Agterberg, Arxiv: 1912.09525 (2019).
- [54] A. Suter and B. Wojek, *Phys. Procedia* **30**, 69 (<http://lmu.web.psi.ch/musrfit/user/html/user>) (2012).
- [55] A. Maisuradze, R. Khasanov, A. Shengelaya, and H. Keller, *J. Phys.: Condens. Matter* **21**, 075701 (2009).
- [56] C. W. Clawson, K. M. Crowe, S. S. Rosenblum, S. E. Kohn, C. Y. Huang, J. L. Smith, and J. H.

Brewer, Phys. Rev. Lett. **51**, 114 (1983).

[57] B. E. H., Physical Review B **68**, 054506 (2003).